

Characterisation of LCF Performance of X100 Weld-Joints: Mechanistic Yield Strength Modelling, Finite Element Analyses and DIC Testing

D.J. Long^{1,2}, R.J. Devaney^{1,2}, P.E. O'Donoghue^{1,2}, H. Song³, R.A. Barrett^{1,2,4*}, S.B. Leen^{1,2,4*}

¹College of Science and Engineering, National University of Ireland Galway, Ireland.

²Ryan Institute for Marine, Environment and Energy, NUI Galway, Ireland.

³Sino-European Institute of Aviation Engineering, Civil Aviation University of China, China

⁴SFI I-Form Advanced Manufacturing Research Centre, Ireland.

*Joint senior author.

Abstract

This paper is concerned with the effect of welding on the fatigue behaviour of X100 material for steel catenary risers. The methodology includes both modelling and experimental characterisation. The modelling combines (i) a physically-based yield strength model to capture the thermally-induced microstructural heterogeneity and associated spatial variations in relative contributions of the key strengthening mechanisms due to welding, and (ii) a five-material cyclic plasticity model with a Coffin-Manson strain-life fatigue model for prediction of cross-weld heterogeneity in cyclic plasticity and fatigue response. The combined non-linear isotropic-kinematic cyclic plasticity behaviour of the five weld joint constituent materials (PM, weld metal (WM) and heat-affected zone (HAZ) subregions) is implemented via a user material (UMAT) subroutine, including Kocks-Mecking monotonic-cyclic evolution of yield stress. The experimental methodology consists of tensile tests with digital image correlation (DIC) for X100 PM and cross-weld samples. The results indicate that the primary phenomenon driving the detrimental effect of welding on fatigue is the evolution of cyclic strain localisation in the ICHAZ, leading to predicted ICHAZ failure.

1. Introduction

With the depletion of earth's natural resources, it is becoming increasingly challenging to source hydrocarbon fuels, namely oil and natural gas. For offshore hydrocarbon recovery, current trends indicate the move towards deepwater, and in some cases ultra-deepwater, due to the exhaustion of shallow water resources. Water depths are typically categorised as follows:

shallow (< 125 metres), deepwater (125 – 1500 metres), and ultra-deepwater (> 1500 metres). Offshore platforms for oil and gas production in shallow waters are generally fixed to the seabed and are known as fixed platforms. However, with increasing water depths, fixed platforms are not feasible, and are generally replaced by floating platforms. Due to the added complexity of a floating platform and increased riser length, significant costs are associated with the transition towards deepwater. Steel catenary risers (SCRs) are the preferred solution for deepwater hydrocarbon recovery, owing to their cost effectiveness when compared with flexible risers, for example. Modern SCRs are freely suspended with no intermediate buoys for support and are manufactured using a high strength steel such that they can resist self-weight and dynamic loads. With the industry's continuous move towards greater water depths, there is an associated trend to opt for higher strength steels for the manufacture of SCRs. While the rise in cost associated with higher steel grades is significant, there is an associated cost-benefit for manufacturing SCRs [1]; this is due to reduced wall thickness requirements with high strength steels, and hence reduced material requirements. However, with the introduction of next-generation materials and reduced pipeline wall thicknesses, greater uncertainty lies with the structural integrity of welded connections, particularly in terms of fatigue performance. It is understood that due to the variation in microstructural characteristics across the weld-joints, particularly within the HAZ, there is a variation of material properties and constitutive behaviour, which leads to non-uniform and localised strain distributions under cyclic loading; potentially leading to diminished fatigue performance.

Inhomogeneous strain distributions are thought to be the root cause of reduced fatigue life in weldments particularly for LCF. Previous work by Devaney [2], [3] has suggested that the knockdown in fatigue life associated with welded connections is due to inhomogeneity in constitutive behaviour leading to strain localisation in softer welding-affected regions, e.g. ICHAZ, rather than specifically, inhomogeneity in fatigue behaviour. Although it is possible to represent a welded joint as composed of a number of discrete weld-affected zones, such as PM, ICHAZ, FGHAZ, CGHAZ, and WM, this is clearly an idealisation. In fact, there is a complex variation in welding-induced microstructural features across the welded joint. Barrett et al. [4] presented a physically-based constitutive model for homogeneous materials, which, with an understanding of the variation in microstructural characteristics across a welded joint may be applied to gain insight into the effect of welding on material performance, and hence, through-process modelling of welding, such as in the work of Mac Ardghail et al. [5]. Touboul et al. [6] presented a detailed DIC test programme to characterise the phenomenological

viscoplastic behaviour of a P91 steel welded joint at room temperature, and at 625 °C, by discretisation of the regions of the PM, HAZ and WM; this approach proved useful for FE modelling of the welded connection, highlighting the effect of the heterogeneous material property distribution. However, the main limitation of this approach is that changes to the welding process would require additional experimental work. Similarly, Farragher [7] conducted P91 cross-weld fatigue tests to characterise the cyclic (phenomenological) viscoplastic material parameters, which were used in three-material cross-weld FE models for validation, i.e. the HAZ was treated as a homogeneous material. In contrast, via application of through-process simulation of the multi-pass welding process, e.g. Mac Ardghail et al. [5], prediction of the continuous distribution of microstructural characteristics and associated mechanical behaviour across a welded joint was carried out for welding process optimisation. Hyde and Sun [8] presented work which describes a procedure for determining the high temperature creep properties for each sub-region of welds from experimental results, and also presented a creep damage mechanics approach in FE analyses which could predict subsequent failure of welds, with application to P92 welded joints. Ren et al. [9] conducted experiments with DIC which was used to investigate the strain distribution for a steel plate weld joint for estimation of LCF performance. Using the results, a nonlinear strain model was presented for fatigue life prediction using two key metrics from the experimental work: peak strain and strain-rate. Veerababu et al. [10] investigated the LCF behaviour of tungsten-alloyed 9Cr steel (P92) welded joints and PM. The fully reversed LCF tests were conducted at 550 °C for high-temperature applications at a constant strain-rate. It was found that the welded joint samples exhibited a lower stress response than that of the pure PM for low strain amplitudes, and that the welded joint exhibited a significantly lower fatigue life. However, at higher strain amplitudes, the weld joint and PM exhibited similar fatigue life.

This paper firstly presents a mechanistic yield stress (YS) model is presented for (i) analysis of the thermally-induced microstructural changes during the welding process, and (ii) prediction of the local variations in the relative contributions of the major strengthening mechanisms. The model is applied to X100 parent metal (PM), physically-simulated fine-grain heat-affected zone (FGHAZ) material, and to inter-critical heat-affected zone (ICHAZ) material, including the effects of cooling rate. The model predicts that precipitate and high-angle boundary strengthening mechanisms are dominant factors affecting variation of YS across the welding-affected zones at room temperature. Secondly, tensile experimental tests are conducted in conjunction with digital image correlation (DIC) for X100 PM and cross-weld samples. The

DIC results show failure in the cross-weld tests within the WM region due to initial softening, subsequent necking and cracking. A multi-material finite element model is shown to effectively capture the strain distribution of the DIC full-field strain maps at low strain levels. Finally, the factors which cause reduced fatigue life performance in X100 weld-joints are investigated using the five-material finite element model, representative of a real X100 cross-weld. The combined non-linear isotropic-kinematic cyclic plasticity behaviour of the five weld joint constituent materials (PM, weld metal (WM) and heat-affected zone (HAZ) subregions) is implemented in the finite element model via a user material (UMAT) subroutine, including Kocks-Mecking monotonic-cyclic evolution of yield stress. A low-cycle fatigue (LCF) case study of the welded joint is conducted, using measured Coffin-Manson data for each zone. The model indicates that the primary phenomenon driving the detrimental effect of welding on fatigue is the evolution of cyclic strain localisation in the ICHAZ, leading to predicted ICHAZ failure. This is despite the ICHAZ displaying the strongest Coffin-Manson strain-life behaviour of the weld-affected zones.

2. Methodology

2.1. Mechanistic yield strength model

To model the YS of X100 PM and other weld-joint constituent materials, a bottom-up approach is taken [11]. Hence, for steels, this involves modelling the YS of the primary material, iron and adding the other strengthening contributions. A metallic alloy's YS can be considered to consist of two distinct contributions, due to the presence of (i) dislocations and (ii) obstacles, such as particles and boundaries, which are combined using a root mean square approach [12], as follows:

$$\sigma_y = M \cdot \sqrt{\tau_A^2 + \tau_B^2} \quad (1)$$

where M is the Taylor factor. The root mean square approach explicitly assumes that mechanisms (i) and (ii) do not interact, and that the sets of discrete obstacles are of identical strengths. Preliminary calculations for the YS of X100 PM have shown that dislocation strengthening (i) is equal to just 20% of the overall YS. Hence, the YS model presented here comprises a linear summation of the individual strengthening contributions, excluding the addition of dislocation strengthening, as this effect is captured by the grain boundary

strengthening effect. The contribution due to dislocations, τ_A is modelled using the Taylor relation, as follows:

$$\tau_A = \alpha\mu b\sqrt{\rho} \quad (2)$$

where μ is shear modulus, b is Burgers vector magnitude, and ρ is dislocation density. α is a material-specific constant, taken as 0.3 for iron and steels [13]. The YS contribution due to the presence of obstacles to dislocation motion, or in this case, the total YS is modelled by summation of the individual strengthening contributions:

$$\sigma_y = \tau_B = \tau^* + \tau_b + \tau_{ss} + \tau_{pr} \quad (3)$$

where τ^* is thermal stress, τ_b is boundary strengthening, τ_{ss} accounts for substitutional and interstitial solid solution strengthening, and τ_{pr} is the precipitate strengthening contribution. The thermal stress arises from short-range (thermal) obstacles which can be surmounted by thermal fluctuations, and can be modelled using an Arrhenius slip-rule type approach [14]:

$$\tau^* = \frac{k_B T}{v} \cdot \left(\ln \left(\frac{\dot{\epsilon}_0}{\dot{\epsilon}} \right) + \frac{q}{k_B T} \right) \quad (4)$$

where k_B is Boltzmann constant, v is activation volume, $\dot{\epsilon}_0$ is the rate constant, q is activation energy (Helmholtz free energy) and T and $\dot{\epsilon}$ are temperature and strain-rate, respectively. In bainitic steels, boundary strengthening is from two boundary types: high-angle boundaries (HABs) and low-angle boundaries (LABs), giving $\tau_b = \tau_{HAB} + \tau_{LAB}$. The HAB contribution is modelled using the classic Hall-Petch relation, where grain size is defined using the smallest HAB dimension, i.e. block size in bainite. In X100, LABs are formed between laths, where LAB's are defined as having crystallographic misorientation of $< 15^\circ$. LAB strengthening is modelled assuming inverse proportionality to effective lath width, \bar{m} [15]:

$$\tau_{LAB} = \frac{\alpha_2 \mu b}{\bar{m}} \quad (5)$$

where α_2 is a constant between 2 and 3 [16]. The Naylor mean slip length model is used to determine effective lath width:

$$\bar{m} = \frac{2}{\pi} \left[w \cdot \ln \left(\tan \left(\arccos \left(\frac{w}{l} \right) \right) + \frac{l}{w} \right) + l \left(\frac{\pi}{2} - \arccos \left(\frac{w}{l} \right) \right) \right] \quad (6)$$

where w and l are lath width and length, respectively. Block diameters and lath widths are measured using EBSD scans of X100 PM and FGHAZ materials with the line intercept method

using the *MTEX* package with *Matlab*. Like boundary strengthening, solid solution strengthening is comprised of contributions from two sources: elements in interstitial and substitutional solid solution. Interstitial solid solution strengthening due to the presence of carbon is modelled using a power-law fit to carbon steel YS data from the American Iron and Steel Institute (AISI), as shown in Figure 1.

Substitutional solid solution strengthening is modelled using the statistical Labusch-Nabarro model [17] for each alloying element, as follows:

$$\tau_{\text{LN}} = \frac{(2pf_m^4c^2)^{1/3}}{2b^{7/3}(\mu b^2)^{1/3}} \quad (7)$$

where p is the range in which the maximum interaction force, f_m is effective, and c is solute concentration. It is assumed that the dislocation must move 2 to 3 lattice spacings for yielding to occur [16], giving $p = 3a$. f_m is calculated as a function of lattice parameter and modulus mismatch between iron and the solute atom [17]. Lastly, precipitate strengthening is modelled using the Ashby-Orowan equation [18], as follows:

$$\tau_{\text{pr}} = \frac{0.093\mu b f_v^2}{r} \ln\left(\frac{r}{b}\right) \quad (8)$$

where f_v and r are precipitate volume fraction and radius, respectively. Precipitate phases and key characteristics are quantified in this work using thermodynamic simulation software, *MatCalc* with precipitation kinetics simulations. X100's initial heat treatment and chemical composition are used as inputs to determine details of PM precipitates, followed by additional simulations with FGHAZ thermal histories at two different cooling rates.

2.2. Experimental testing

An experimental test programme is devised which is aimed at (i) characterising the effect of welding on the tensile behaviour on X100 PM, (ii) assessing if strain-rate has some significant effect on the tensile behaviour of X100 PM and welded joints, and (iii) using DIC to determine the full-field strain distribution for X100 welded joints under tensile loading, for validation of a FE modelling methodology. The tensile tests are conducted using an Instron 4467, which is a uniaxial test machine. The cross-head, which applies a load to the test specimen at specified control speeds, is screw-driven, and is powered by an electric DC servomotor.

Figure 2 shows the installed tensile test specimen within the jaw grips of the Instron test machine. It also shows how the DIC equipment is used in conjunction with the Instron test machine. ARAMIS DIC equipment is used; the stereo sensor setup is placed on a tripod oriented orthogonal to the face of the test specimen. The stereo sensor setup allows for more precise 3D full-field strain maps to be produced, i.e. strains in the z-direction (thickness direction) are computed. DIC has been used extensively in recent years for contactless deformation measurements. Many factors affect the performance of DIC, including calculation parameters, subpixel interpolation schemes, image noise, system resolution, speckle quality, and the test environment [19]. These are the factors which influence pattern quality. In this work, a speckle pattern is applied to the surface of each test specimen, which the ARAMIS Professional software uses to track displacements. A surface component (area of sample over which measurements are taken) is produced, which is comprised of measurement points, arranged in a triangular fashion. Using information from sensor calibration (prior to testing), the software determines the spatial coordinates of the origin from the corresponding image points, i.e. the speckle pattern. Strains are calculated at sets of measurement points, described as neighbourhoods, resulting in an overdetermined set of equations, illustrated in Figure 3.

Strains are calculated in local coordinates, which move with the material. Thus, each measurement point has its own moving (local) coordinate system. The true strain at each local coordinate system is calculated using the local stretch tensor, as follows:

$$\mathbf{U} = \begin{bmatrix} \Lambda_x & \Lambda_{xy} \\ \Lambda_{yx} & \Lambda_y \end{bmatrix} = \begin{bmatrix} \varepsilon_x + 1 & \varepsilon_{xy} \\ \varepsilon_{yx} & \varepsilon_y + 1 \end{bmatrix},$$

where true strain is given as

$$\varepsilon' = \ln(\Lambda) = \ln(\varepsilon + 1)$$

where ε represents so-called engineering strain. Conventionally, DIC speckle patterns for tensile tests are generated using speckles of black spray paint on a white background. It has been noted by Chen et al. [19] that the optimal DIC speckle characteristics are an equivalent speckle diameter of five pixels and a speckle coverage of between 50% and 70%. However, producing an optimised speckle pattern with this method is problematic due to lack of control over the process. Hence, a novel computerised method is developed for flat samples, such that the pattern coverage and speckle diameter can be controlled. *Speckle Generator*, a software package from Correlated Solutions is used to create a digital speckle pattern with a coverage of 65%, and speckle diameter of 0.1 millimetres, as shown in Figure 4.

Based on the speckle diameter of 0.1 millimetres used in this work, an optimised facet size of 0.5 millimetres is implemented within the software – this governs the resolution of the DIC measurements, and hence, the accuracy. Therefore, over the area of the gauge region, the DIC measurements here are capable of capturing mean strains. Based on a resolution of 0.5 millimetres, local strains are captured with a satisfactory degree of accuracy.

Flat tensile test specimens are manufactured according to ASTM E606 test standard. The technical specification for the samples is given in Figure 5.

The X100 cross-weld test specimens are cut from as-received X100 pipe girth welds. The location of the gauge region for each cross-weld sample, with respect to the location of the constituent materials of the weld-joint is a crucial factor in influencing the test results. It was decided that, due to the bevel-shape of the weld-joint (see Figure 6), the fusion zone of the weld should lie at the centre of the gauge region, hence providing adequate strain distribution data for each of the constituent materials.

In total, three PM test samples and two cross-weld samples are manufactured and tested, as per the test programme outlined in Table 1. The PM samples are tested according to two different cross-head speeds, to qualitatively assess the effect of strain-rate on material behaviour (using constant cross-head speed as a proxy for constant strain-rate). Similarly, two different cross-head speeds are used to test the cross-weld samples. In each case, the DIC sample frequency is compared with the point sample frequency from the tensile test machine; this is used for correlation of DIC strain data with tensile test stress data.

2.3. Representative finite element model

A FE model, representative of the real X100 cross-weld used in these tests is constructed for validation of the mixed-material interface FE model methodology used in the previous section. Here, the material properties are defined using real monotonic test data with ABAQUS' built in isotropic model from the work of Devaney [2], [3] for PM, simulated FGHAZ, and simulated ICHAZ, Song [20] for WM based on DIC test results, and approximate CGHAZ test data obtained from the work of Dancette [21] for welded DP980 steel. A schematic of the geometry assumed for the cross-weld FE model is shown in Figure 7, along with a high-contrast DIC strain field of a real X100 weld-joint.

A boundary condition is applied in the x-direction to the model, at a single node to prevent rigid body motion in the x-direction. The bottom edge of the model is constrained in the y-

direction and relative displacement is applied to the top edge. The scale of the model is defined by the dimensions of the gauge region, and measures 17.5 millimetres in length, and 7.5 millimetres in width. The thicknesses of the regions of the HAZ are inferred using the X100 cross-weld nanoindentation hardness trace, from Devaney [2]. The model is discretised using eight-node biquadratic plane strain quadrilateral, reduced integration elements (CPE8R) in ABAQUS. A structured quadrilateral element mesh is applied within the sub-zones of the HAZ, and an unstructured quadrilateral element mesh is used in the PM and WM regions, which ensures that elements are not distorted due to the angle of weld. Seed bias is applied to the PM and WM regions, with reducing element length towards interfaces of the HAZ, to ensure that deformation is captured accurately at mixed material interfaces. A mesh refinement study is conducted to ensure a precise solution is obtained.

2.4. Constitutive modelling

A phenomenological constitutive model was fitted to capture the LCF behaviour of X100 and its weld joint constituents, using the experimental test data from Devaney [2], [22]. It is clear from the LCF test data that X100 PM undergoes non-linear cyclic softening, since the peak stress at the end of each cycle is gradually reduced. This phenomenon is best described by the non-linear isotropic hardening (softening) model. The gradual change in peak stress is accounted for in the model by expansion or contraction of the yield surface, which is described using the Von Mises yield criterion. For implementation of both kinematic hardening and isotropic softening of the weld joint constituent materials, the yield functions of each are combined to form the following expression [23]:

$$f = \left(\frac{3}{2} (\boldsymbol{\sigma}' - \boldsymbol{x}) : (\boldsymbol{\sigma}' - \boldsymbol{x}) \right)^{1/2} - r(p) - k_0 \quad (9)$$

where f is the yield function, $\boldsymbol{\sigma}'$ is the deviatoric stress tensor, \boldsymbol{x} is the kinematic back stress tensor, $r(p)$ is the isotropic softening term, which is a function of cumulative plastic strain, and k_0 is the cyclic YS term. The yield criterion is as follows: for $f < 0$, the material has not yielded, and for $f = 0$, the material has yielded. The isotropic softening term is governed by the following expression, where b and Q are constants:

$$r(p) = Q(1 - e^{-bp}) \quad (10)$$

b governs the rate of softening, while the magnitude of Q determines the saturation stress. Similarly, uniaxial kinematic hardening is controlled by the following expression, where c and γ are fitted constants:

$$x = \frac{c}{\gamma} (1 - e^{-\gamma \varepsilon_p}) \quad (11)$$

Here, x varies as a function of plastic strain, ε_p , as opposed to p , since kinematic hardening is independent of cycle number. A key motivation for the kinematic hardening model under cyclic loading is the occurrence of the Bauschinger effect. The Bauschinger effect is the phenomenon whereby the tensile plastic strain leads to a reduced subsequent compressive YS and vice versa [14], [23], [24]. During the transition from monotonic to cyclic loading, there is also a transition in the YS term. The YS term used in cyclic models, referred to as k_0 does not accurately represent the true yield stress of the material, and is rather, a fitted parameter in a constitutive model. To account for this, YS evolution is considered in this model, which gives a more precise fit to the first cycle experimental data for various materials. YS evolution is executed here using the Kocks-Mecking dislocation density evolution model. As such, the phenomenological YS is defined in part by physical parameters, as follows:

$$k_0 = \sigma_0 + M\alpha\mu b\rho^{1/2} \quad (12)$$

where the latter is the Taylor hardening model, given by Equation 3.2, and σ_0 is a term used to denote the summation of all other yield stress contributors. Hence, dislocation density evolution gives rise to yield stress evolution as a function of accumulated plastic strain. The Kocks-Mecking dislocation density evolution model is as follows:

$$\frac{d\rho}{dp} = \frac{k_1}{b}\rho - k_2\sqrt{\rho} \quad (13)$$

where ρ , p , and b have their usual meanings and k_1 and k_2 are fitted constants. Through estimating the evolution of yield stress by comparison of monotonic and cyclic loading curves, constants k_1 and k_2 are fitted for each material from the experimental work of Devaney [2]. For identification of fatigue life performance, and later prediction, the common Coffin-Manson model is fitted to weld-joint constituent materials, and is given by:

$$\frac{\Delta\varepsilon_p}{2} = \varepsilon'_f (2N)^c \quad (14)$$

where ε'_f and c are the fatigue ductility coefficient and exponent, respectively. ε'_f and c are fitted constants, where ε'_f is defined by the strain at the intercept at $2N = 1$.

2.5. Finite element model for low-cycle fatigue

As per the FE model presented in Section 2.3 of this paper, a 2D FE model is constructed to represent a simple X100 welded joint, with the weld in the direction transverse to the loading

direction. The PM, WM, FGHAZ (physically-simulated), and ICHAZ (physically-simulated) region material behaviour are modelled, as described in Section 2.4, using LCF experimental data from Devaney [2]. Due to the non-availability of CGHAZ test data, published monotonic test data for DP980 steel (with similar chemical composition to X100) from Dancette et al. [21] is used to model the monotonic behaviour. The model is set up in a displacement-controlled manner, to simulate the effects of LCF on the cross-weld joint. Using symmetry, half of the welded joint is modelled, such that a constraint may be applied orthogonal to one edge. The basic FE model setup used here is illustrated in Figure 8, indicating the boundary conditions and geometry of the model.

A boundary condition is applied in the x-direction to the model, along the right-hand edge; this is used to represent symmetry within the model, and also prevents rigid body motion in the x-direction. A boundary condition is applied to the bottom edge of the model such that a relative displacement can be applied to the top edge, resulting in a strain in the y-direction. The scale of the overall welded joint is six millimetres in width (x-direction) and ten millimetres in length (y-direction), and hence the width of the specimen in the FE model is three millimetres. The length of each of the HAZ sub-regions are inferred using and scaled down from the X100 cross-weld nanoindentation hardness trace, as per the work of Devaney [2], [3]. As before, a mesh refinement study is conducted to ensure a precise solution is obtained. For definition of material properties within the FE model, a UMAT subroutine is written. The UMAT subroutine is comprised of a NLKIH model and Kocks-Mecking dislocation density evolution model, as described in the previous section. The subroutine is written for plane strain elements, and uses an implicit integration scheme to solve the plasticity equations.

3. Results

3.1. Parameter identification

The mechanistic YS model parameters identified in this work are based on microscopy and microstructure-sensitive test methods, e.g. tensile tests for various known microstructures including those of pure iron, ferritic carbon steel and X100. To characterise the variables in the thermal stress equation, Sakui's data [25], [26] is used, for lower the yield stress of pure iron at a range of temperatures, strain-rates and grain diameters. A low dislocation density of $1 \times 10^6 \text{ mm}^{-2}$ is assumed due to the high iron purity, giving a Taylor shear stress contribution of approximately 6 MPa. The Taylor factor of $M = 2.9$ is adopted. The following values for the activation energy and natural logarithm of the rate constant are found to give the best fit,

respectively: 0.44 and 7.5. This is in reasonable agreement with published data. In a study which investigated the effect of temperature and strain-rate on the flow stress of pure iron crystals [27], activation energy was found to lie between 0.47 and 0.58 eV, and the natural logarithm of the rate constant was found to lie between 7.0 and 11.0.

The temperature dependence of the Hall-Petch constant is determined using the experimental data of Sakui [26]. A discontinuity function is used to describe the transition in behaviour of k_{HP} from a constant to exponential decay with respect to an increase in temperature, as follows:

$$T < 390 \text{ K: } k_{HP} = k_1 \text{ N/mm}^{-3/2} \quad (15)$$

$$T \geq 390 \text{ K: } k_{HP} = k_2 \cdot \exp\left(-\frac{T}{T_x}\right) \text{ N/mm}^{-3/2} \quad (16)$$

where k_1 is equal to 20, k_2 is equal to 110, and T_x is equal to 227. For boundary strengthening models, EBSD data from [2] is used for estimation of mean block diameter and lath width. For materials with hierarchical microstructures, such as X100, HAB diameter can be assumed to be governed by the lowest HAB dimension, which in this case is the block width. For X100 PM and the two FGHAZ cases, this parameter is estimated from EBSD images to characterise mean block areas for each sample. Table 2 shows estimated block diameter and lath width values for the PM, FGHAZ (10 K/s), and FGHAZ (30 K/s) materials.

In this work, a non-linear kinematic hardening model is employed to capture the initial monotonic hardening behaviour of X100 weld joint constituent materials. Like the isotropic hardening model, the kinematic hardening model reaches a peak stress at a given plastic strain; this peak stress is fitted according to the ultimate tensile strength (UTS) of the material. Kinematic hardening stress saturation is defined as the ratio of the fitted constants, $\frac{c}{\gamma}$. Hence, $\frac{c}{\gamma}$ is defined as the difference in magnitude between the UTS and k_0 . With this, the parameters are fitted to experimental data using Equation 11.

Figure 9 (b) shows that the kinematic hardening model is fitted to experimental plastic strain and stress data. Here, the stress is defined as the magnitude of stress at the given plastic strain minus the cyclic YS. In this work, the kinematic hardening terms are fitted whilst neglecting the effect of isotropic softening, due to its relative insensitivity to plastic strain. For both the kinematic and isotropic hardening models, it is found that the best fit to the experimental data is obtained using superposition of two terms. The fitted parameters for the NLKIH and Kocks-Mecking models are presented in Table 3. Initial dislocation density, ρ_0 is presented for each

material to satisfy the initial condition for the differential dislocation density evolution equation.

The models are evaluated at various strain ranges to ensure that the constitutive response is characterised for any given LCF simulation. Due to the closely related grain size in CGHAZ, and ICHAZ, the isotropic softening behaviour of the CGHAZ is modelled using fitted constants for the ICHAZ material. The resulting fit to PM LCF data is presented in Figure 10 for a strain-range of 1.2%.

Similarly, the modelled responses for WM, FGHAZ, and ICHAZ are presented in Figure 11.

The two parameters required to fit a Coffin-Manson model are the applied plastic strain-range and the number of cycles to failure. Using LCF test data from Devaney's work [2], [3], plastic strain-ranges are estimated for tests carried out which were controlled at four different strain-ranges: 0.6%, 0.8%, 1.0%, and 1.2%. Since the plastic strain-range is not constant for the materials during testing, due to cyclic softening, the average plastic strain-ranges are used to fit the Coffin-Manson models. The fitted Coffin-Manson constants are presented in Table 4.

The fitted Coffin-Manson parameters in Table 4 indicate that the FGHAZ material has the highest fatigue ductility coefficient, and that PM has the lowest. The FGHAZ also has the highest fatigue ductility exponent, by magnitude, whilst the ICHAZ has the lowest. The fitted results from Table 4 and experimental data points are presented, graphically in Figure 12.

3.2. Mechanistic yield stress

In the absence of published strain-rate and temperature data for X100, the predicted effects of temperature and strain-rate for X100 are compared to published experimental data for S35C steel (a high-strength offshore steel, with a chemical composition similar to X100) across a range of temperatures and for two contrasting strain-rates of 0.1 s^{-1} and 450 s^{-1} [28] in Figure 13; YS data is presented in terms of a YS reduction ratio, defined here as $YSRR = \frac{\sigma_y^{273K}}{\sigma_y^T}$, where σ_y^{273K} is the YS at 273 K and σ_y^T is the YS at any other temperature (for the given strain-rate). Excellent agreement is observed across the entire temperature range for the higher strain-rate, and up to 473 K for the lower strain-rate; the model over-predicts YSRR (by less than 20%) above 473 K for the latter.

Figure 14 shows a comparison of the contributions from the most significant strengthening mechanisms for PM and FGHAZ.

In each case, the primary YS contributors are HAB and precipitate strengthening, accounting for between 20 and 30% of the total yield stresses each. Other major contributing strengthening mechanisms include Taylor hardening, LAB strengthening and interstitial solid solution strengthening (except for in FGHAZ (10 K/s) due to additional cementite formation). The substitutional solid solution strengthening contribution is found to be relatively small (< 5%), due to the low concentrations of substitutional alloys. Similarly, the thermal stress contribution is found to be relatively small (< 4%) in each of the materials, which is in part attributed to the low to intermediate strain-rates considered here.

Figure 15 shows a comparison of the predicted yield stresses (0.1% offset and nanoindentation-based YS with a scaling factor of $Z = 4.5$) and measured data for the PM and FGHAZ materials, as well as comparison between predicted and measured data for the ICHAZ. It is necessary to use approximations for some of the physically-based parameters due to non-availability of EBSD characterisation for ICHAZ. The highest predicted YS is associated with the FGHAZ (30 K/s) material, followed by the FGHAZ (10 K/s) and PM. A significant reduction in YS is predicted in the ICHAZ due primarily to increased block diameter and lath width, relative to the PM. Reasonable correlation between the predicted and tensile proof stress of PM and FGHAZ (10 K/s) is shown, compared with FGHAZ (30 K/s) and ICHAZ which over-predict their tensile proof stresses significantly.

3.3. Experimental test results

Figure 16 shows the tensile response for X100 PM at different cross-head speeds, including one repeat test (tests PM1, PM2, and PM3).

Discrepancies are visible between tests PM1 and PM2 in the strain range 1-5%. A significantly higher UTS value is observed in test PM2. However, in comparing tests PM2 and PM3, the primary difference is a higher flow stress for the faster cross-head speed. Test results from tests CW1 and CW2, at different cross-head speeds are presented in Figure 17.

The higher cross-head speed gives an increased UTS and fracture strain, but a reduced yield stress. However, possible manufacturing variations between the cross-weld samples with respect to weld joint location etc., may be the cause of these variations in tensile response. The key material properties obtained from the stress-strain curves are presented in Table 5.

Clearly, the data in Table 5 indicates that an increase in cross-head speed causes an increased PM YS and UTS. There is no clear trend in relation to the level of elongation, however. In

contrast, the increased cross-head speed in the cross-weld tests results in a reduced yield stress, with an increase in UTS. Notable differences between PM and cross-weld samples are that PM samples have a much higher yield stress and UTS, whilst cross-weld samples undergo higher levels of elongation before fracture. Figure 18 shows the DIC strain maps for test PM1 at various applied strains, (a) 5%, (b) 10%, (c) 15%, and (d) 20%, with the corresponding points indicated on the stress-strain curve. The results clearly show the onset of non-uniform elongation and necking within the central region of the specimen at (b). This is followed by subsequent strain localisation and necking, leading to ductile fracture.

3.4. Monotonic test simulation

The results of the FE model simulation are presented and compared with DIC results for small strains (compared with total elongation). Due to the unavailability of high-strain tensile data for CGHAZ and WM materials, the FE model is limited to strain of up to 2%. The loading direction strain distribution from the simulation is compared with the DIC strain distribution in Figure 19 for an applied strain of 1.5%.

The FE model is seen to broadly capture the inhomogeneity in strain distribution across the cross-weld sample. The FE weld angle appears to cause a different orientation of strain bands compared to the actual weld-joint. Another key difference is the occurrence of a localisation of strain shown in the bottom-left of the actual weld-joint; the FE model shows a similar localisation, but at a slightly different location. The actual weld-joint does not show any evidence for three distinct HAZ sub-zones as idealised in the FE model. Rather, it shows a more continuous transition from low strain (PM) to higher strain (WM). The comparison for an applied strain of 2% is shown in Figure 20.

In this case, the FE model and DIC show greater similarity. Strain localisation along the bottom edge of the WM is predicted by the model, which is found within the DIC test result also. Upon closer inspection, the FE model is also shown to effectively capture strain localisation at what is suspected to be the WM-CGHAZ interface on the right-hand side in the real monotonic test. The DIC-based and modelled strain distributions are plotted and compared at an applied strain of 1.5% along the left edge of the gauge region in Figure 21.

There is general agreement between the strain distributions, though there appear to be differences between the FE model and DIC in terms of apparent demarcations of the idealised HAZ sub-zones. The demarcation of sub-zones is naturally much less distinct in the experimental sample, whereas the simulation shows clear strain localisation at the material

interfaces. The HAZ sub-zone boundaries are shown in red for the model, and in black, as estimated from DIC.

3.5. Low-cycle fatigue simulation

Loading direction tensile strain distribution results from the 1% strain-range LCF FE model simulation at various cycle numbers (for the tensile part of the cycle) are presented in Figure 22.

Figure 22 indicates that beginning at the first cycle, there is an inhomogeneous strain distribution in the loading direction due to heterogeneity of material behaviour. With an increase in cycle number, there is re-distribution of strain throughout the cross-weld. From parts (c) to (d), it becomes apparent that strain localises increasingly in specific regions with increasing cycle number. Figure 23 presents the strain distribution in the cross-weld in greater detail at $N = 50$ cycles, with the weld joint constituent materials visibly distinguished.

This shows significant strain localisation within the ICHAZ material, which appears to propagate from the edge of the weld, at the ICHAZ-FGHAZ interface. The contour plot indicates that the peak strain within the ICHAZ exceeds 1.5%, which is more than three times greater than the bulk applied tensile strain of 0.5%. Other than strain localisation, another factor which can significantly influence fatigue performance is the mean stress; tensile residual stresses are detrimental to fatigue life performance (due to the mean stress being > 0), as they increase the fatigue crack propagation rate and accelerate fatigue crack initiation [29], [30]. The tensile stress distribution is plotted in Figure 24 for the compressive portion of cycle number 50.

This effect is caused by ratcheting within regions of the ICHAZ material, whereby the stress-strain hysteresis loop is translated towards the tensile region of the stress-strain plot. To evaluate and compare the stress-strain response for each of the weld joint constituent materials, sample stabilised hysteresis loops at peak strain locations are plotted and compared at cycle number 100 in Figure 25 for each sub-zone of the model.

This indicates that highest strain localisation occurs within the ICHAZ, with a cyclic strain concentration factor of almost 2. While not as severe as in the ICHAZ, significant strain localisation in the WM is also shown by the model. Lastly, similar responses are observed for PM and FGHAZ, which exhibit a strain-range of less than the total applied value of 1%. Using these stress-strain profiles, the maximum plastic strain range is calculated for each material

sub-zone and is used to estimate the local fatigue-life of each material with the fitted Coffin-Manson models, as shown in Table 6. This shows the calculated stabilised maximum plastic strain-ranges for each of the weld joint constituent materials. It indicates the localisation of plastic strain within the ICHAZ and WM. The local Coffin-Manson fatigue life predictions based on the corresponding plastic strain ranges indicate a stark difference in fatigue life performance between each of the zones. The lowest local fatigue life prediction is in the ICHAZ, which is predicted to fail at just 777 cycles, followed by WM, which is predicted to fail at 1003 cycles. The least likely failure location is within the FGHAZ, which is due to the low plastic strain-range. PM is second least likely to cause failure, with a predicted number of cycles to failure of 12311.

4. Discussion

The YS model predicts the X100 PM YS to within 1% of the measured value. The model also captures the qualitative effects (relative to PM) of the simulated welding thermal cycles for both the FGHAZ and the ICHAZ. Specifically, the model captures the increase for both FGHAZ materials (10 K/s and 30 K/s cooling rates) and more importantly, the decrease in YS value for the ICHAZ material. Differences between the tensile test values of 0.1% proof stress and values inferred from nanoindentation tests suggest that the latter are over-estimates, potentially due to the higher volume fraction of precipitates in the FGHAZ materials, as predicted in this study. Both the tensile test and nanoindentation data indicate a significant reduction in yield stress for the ICHAZ relative to the PM. The tensile test value, which is obtained from simulated (single-pass) ICHAZ material, indicates a detrimental reduction in YS of more than 40%, relative to the PM. The nanoindentation test, which was conducted on as-welded (multi-pass) ICHAZ, indicates a less detrimental, but nonetheless significant, reduction of about 21%. The YS model results for ICHAZ capture the detrimental effect on YS; the model under-predicts the reduction relative to the tensile test (proof) stress by 24% and over-predicts the reduction relative to the nanoindentation-based stress by just 3%. The model is somewhat representative of both physically-simulated (since single-pass thermal history used in precipitation kinetics simulation) and as-welded (since block diameter estimate from published data was as a result of an extended period elevated temperature transformation, i.e. more representative of multi-pass) ICHAZ materials. Due to the excellent correlation between model and as-welded yield stresses, it is assumed that physically-simulated ICHAZ block diameter is even greater than that used in the model, resulting in further reduction of the YS. This also emphasises the significance of HAB strengthening to the YS of X100. Hence,

predictable differences in physical parameters in different materials allow for the model to predict the YS with a reasonable degree of accuracy.

In comparing uniaxial test results which are conducted at different cross-head speeds, no clear trend is observed in relation to changes in yield stress. This is expected, however, as shown by the YS model, since the thermal stress contribution (which is strain-rate dependent) is negligible in X100 PM at room temperature. The first two PM tests, which are conducted under the same test conditions show significant differences in relation to stress-strain behaviour; most notably, there is a 7% difference in UTS between the two samples, but negligible differences in 0.1% yield stress values and percentage elongation. This difference in stress-strain behaviour is potentially due to local defects within one of the samples. The second PM test, which is conducted at a cross-head speed of 0.35 mm/min shows a yield stress value which is 1.6% greater, and an UTS value which is 4% greater than the third PM test, which is conducted at a lower cross-head speed of 0.035 mm/min. This is as expected for increased strain-rate (cross-head speed), which results in an increased yield stress and flow stress. Differences in percentage elongation here are negligible. The two cross-weld test results show significant differences when compared with PM test results, in terms of yield stress, UTS, and percentage elongation. Firstly, in comparing PM and cross-weld tests (conducted at the same cross-head speed of 0.35 mm/min), it is shown that the PM has a yield stress greater by 34.7%, an UTS which is greater by 27.9%, and the cross-weld test specimen is shown to have a percentage elongation greater by 30%. The lower YS and UTS values of the cross-weld case may be attributed to the lower yield stress and UTS values in WM.

In the cross-weld full-field strain maps, strain localisation is shown initially, prior to the onset of necking to be in the WM region. This is followed by a more clearly localised strain concentration within the WM region, nearer the fusion zone, leading to necking across the WM region, and cracking. This strain localisation is due to the remarkably lower yield stress and UTS within the WM, when compared with PM and other weld-joint constituent materials. This contrasts with the LCF simulation results, where strain localisation apparently occurred in the ICHAZ sub-zone. This was attributed to rapid cyclic softening within the ICHAZ region; such softening does not occur under monotonic loading. According to Devaney [3], cyclic softening within the ICHAZ material is due to lath coarsening. The fusion zone is visibly identifiable from the cross-weld strain maps due to the 'sharp' change in strain across the cross-weld; the identified angle of the cross-weld bevel does not appear to be consistent with the specified angle. This is apparently due to the uneven blending of the fusion zone as a result of the multi-

pass welding process. Also, a notable distinction between the LCF simulation, and the monotonic DIC results, is that the sub-zones of the HAZ are not clearly identifiable from the full-field strain maps. A similar observation can be made from the DIC test results of Touboul et al. [6] for monotonic testing of P91 cross-welds. In relation to the monotonic test simulation, the general DIC strain trends are captured. The strain distributions in the y-direction show reasonable agreement between FE and DIC. Significant differences in the strain are observed within the WM material, where the predicted strain is lower than in the test. This may be the result of several factors relating to the construction of the model. Firstly, the HAZ sub-zone material properties are defined according to test results from physically-simulated materials from the work of Devaney [2]. This is problematic because the physically-simulated materials are based on single pass welding, whereas the tested cross-weld samples are from multi-pass welded pipes; multi-pass welding can affect material properties significantly due to thermally-induced microstructural changes and associated tempering effects within the HAZ sub-zones, compared with single-pass welding; hence, physically-simulated single-pass welds are limited in terms of representing material behaviour within real welds. Overall, the multi-material model proves successful as a modelling methodology for simulation of welded joints subjected to strains up to 2%. Hence, results from the LCF simulation of a simple X100 weld-joint may be taken into consideration.

The LCF case study simulation of a simple plate X100 cross-weld has shown that with an increasing cycle number, significant strain re-distribution is observed, due to variations in yield stress and cyclic softening behaviour of each of the materials. Initially, strain localisation is observed in the WM; however, upon further cyclic loading and strain re-distribution, it is shown that significant strain localisation is observed in the ICHAZ material, increasingly with cycle number until stabilisation. Since WM is the softest material in the welded joint, it is expected that strain localisation should occur there. However, due to the more rapid and extensive cyclic softening shown in the ICHAZ material, strain localisation occurs predominantly in this zone, particularly near the outer edges. The number of cycles to failure is estimated for each of the weld joint constituent materials, excluding CGHAZ using the Coffin-Manson equation. The results show that due to the extensive strain localisation within the ICHAZ, failure is most likely to occur in this zone at 777 cycles (for the given case study), compared with 1003 cycles for WM. This is in agreement with the findings from Devaney's work [2], [3], which has shown in fatigue tests of physically-simulated FGHAZ materials that failure occurs within the interface zone (IFZ), which is representative of the ICHAZ, due to its

location within the sample. The results from the 5-material cross-weld FE model, combined with the results of the physically-based yield strength model, thus provide a mechanistic explanation for the detrimental effect of welding on fatigue, viz. a key phenomenon controlling location and life for fatigue of welded joints is the relative cyclic behaviour, vis-à-vis heterogeneity of microstructure and cyclic plasticity response, leading to complex, cyclically-induced spatial re-distribution of stress and strain across the welded joint. The detrimental effect of welding on fatigue of X100 is clearly illustrated in Figure 26 for both (a) strain-controlled LCF tests (b) load-controlled cross-weld and X100 PM tests compared to X80 PM tests, from Devaney [2]. Clearly, welding causes a fatigue life knockdown of up to two orders of magnitude, relative to PM.

The FE model has also shown that due to a ratcheting effect, tensile residual stresses are accumulated within the ICHAZ; this is another factor which suggests that the failure location in a LCF test is within the ICHAZ, due to the detrimental effect of tensile stresses on LCF performance of materials [30].

5. Conclusions

Based on the work presented in this paper, the following key conclusions are drawn:

- A mechanistic YS model was developed for prediction of YS heterogeneity due to thermally-induced microstructural changes during the simulated welding process, as a basis for a more general technique for more complex multi-pass welding. The model adopts a mechanistic thermal stress model to capture strain-rate and temperature dependence.
- The YS model shows that increased lath width and block diameter in the ICHAZ has a detrimental effect on YS, particularly for physically-simulated ICHAZ, as also reflected by the experimental results. The YS model shows that the most significant strengthening mechanisms in X100 PM and FGHAZ materials are precipitate and boundary strengthening. The presence of finely dispersed precipitates accounts for between 20 to 30% of YS for the weld joint constituents investigated in this study. Precipitates are also a major contributor to YS heterogeneity, as their formation is highly sensitive to changes in temperature and rates of cooling.
- DIC has been used in conjunction with tensile testing to investigate the effect of loading-rate on X100 PM and cross-weld test samples. The measured effect is negligible in terms of YS, UTS, and percentage elongation, due to a very low thermal stress contribution at room temperature. The tensile tests showed that cross-weld YS and UTS values reduced by

34.7%, and 27.9%, respectively, and strain to failure increased by 30%, relative to PM. Hence, welding is shown to have a significant detrimental effect on YS and UTS, but has a beneficial effect on ductility.

- A proposed multi-material FE model of an X100 cross-weld is shown to successfully represent the strain distributions in the X100 cross-weld for total applied strains up to 2%. The simulation results show that strain localisation within the WM region is effectively captured, though the magnitude of strain localisation is not accurately represented.
- The elastic-plastic, multi-material FE model for LCF simulation of the cross-weld has indicated significant cyclic strain re-distribution between the different sub-zones, resulting in a transition from initial dominant strain localisation within WM to most significant strain localisation within the ICHAZ after approximately 50 cycles. ICHAZ is predicted as the failure location, due to significant cyclic strain localisation. In combination with the physically-based modelling, this provides a mechanistic explanation for the detrimental effect of welding on fatigue.

Acknowledgements

This research is funded by Science Foundation Ireland under Grant no. SFI/14/IA/2604. The authors would also like to acknowledge collaborators of the MECHANNICS project.

Data Availability

The raw/processed data required to reproduce these findings cannot be shared at this time as the data also forms part of an ongoing study.

References

- [1] Q. Bai and Y. Bai, *Subsea Pipeline Design, Analysis, and Installation*. 2014.
- [2] R. J. Devaney, "Process-structure-property characterisation of plasticity and fatigue damage in X100 welded joints for steel catenary risers," National University of Ireland, Galway, 2020.
- [3] R. J. Devaney, P. E. O'Donoghue, and S. B. Leen, "Experimental characterisation and computational modelling for cyclic elastic-plastic constitutive behaviour and fatigue damage of X100Q for steel catenary risers," *Int. J. Fatigue*, vol. 116, no. February, pp. 366–378, 2018, doi: 10.1016/j.ijfatigue.2018.06.032.
- [4] R. A. Barrett, P. E. O'Donoghue, and S. B. Leen, "A physically-based constitutive

- model for high temperature microstructural degradation under cyclic deformation,” *Int. J. Fatigue*, vol. 100, pp. 388–406, 2017, doi: 10.1016/j.ijfatigue.2017.03.018.
- [5] P. Mac Ardghail, N. Harrison, and S. B. Leen, “A through-process, thermomechanical model for predicting welding-induced microstructure evolution and post-weld high-temperature fatigue response,” *Int. J. Fatigue*, vol. 112, no. November 2017, pp. 216–232, 2018, doi: 10.1016/j.ijfatigue.2018.02.015.
- [6] M. Touboul, J. Crepin, G. Rousselier, F. Latourte, and S. Leclercq, “Identification of Local Viscoplastic Properties in P91 Welds from Full Field Measurements at Room Temperature and 625 °C,” *Exp. Mech.*, vol. 53, no. 3, pp. 455–468, 2013, doi: 10.1007/s11340-012-9655-8.
- [7] T. Farragher, “Thermomechanical Analysis Of P91 Power Plant Components,” National University of Ireland, Galway, 2013.
- [8] T. Hyde and W. Sun, “Some issues on creep damage modelling of welds with heterogeneous structures,” *Int. J. Mech. Mater. Des.*, vol. 5, no. 4, pp. 327–335, 2009, doi: 10.1007/s10999-009-9105-7.
- [9] X. Ren, X. Xu, C. Jiang, Z. Huang, and X. He, “Strain distribution and fatigue life estimation for steel plate weld joint low cycle fatigue based on DIC,” *Opt. Lasers Eng.*, vol. 124, no. August 2019, 2020, doi: 10.1016/j.optlaseng.2019.105839.
- [10] J. Veerababu, S. Goyal, R. Sandhya, and K. Laha, “Low cycle fatigue behaviour of Grade 92 steel weld joints,” *Int. J. Fatigue*, vol. 105, pp. 60–70, 2017, doi: 10.1016/j.ijfatigue.2017.08.013.
- [11] D. J. Long, R. J. Devaney, S. B. Leen, and R. A. Barrett, “A Mechanistic Yield Strength Model with Application to Welding-Induced Heterogeneity in X100,” *In preparation.*, 2021.
- [12] U. . Kocks, “Thermodynamics and Kinetics of Slip,” *Prog. Mater. Sci.*, vol. 19, pp. 3–275, 1975.
- [13] F. F. Lavrentev, “The type of dislocation interaction as the factor determining work hardening,” *Mater. Sci. Eng.*, vol. 46, no. 2, pp. 191–208, 1980, doi: 10.1016/0025-5416(80)90175-5.
- [14] G. E. Dieter, *Mechanical Metallurgy*, SI Metric. McGraw-Hill, 1988.

- [15] K. Maruyama, K. Sawada, and J. I. Koike, “Strengthening mechanisms of creep resistant tempered martensitic steel,” *ISIJ Int.*, vol. 41, no. 6, pp. 641–653, 2001, doi: 10.2355/isijinternational.41.641.
- [16] R. A. Barrett, P. E. O’Donoghue, and S. B. Leen, “A physically-based high temperature yield strength model for 9Cr steels,” *Mater. Sci. Eng. A*, vol. 730, no. December 2017, pp. 410–424, 2018, doi: 10.1016/j.msea.2018.05.086.
- [17] H. Sieurin, J. Zander, and R. Sandström, “Modelling solid solution hardening in stainless steels,” *Mater. Sci. Eng. A*, vol. 415, no. 1–2, pp. 66–71, 2006, doi: 10.1016/j.msea.2005.09.031.
- [18] Niu Tao, “Precipitation Behaviour and its Strengthening Effect of X100 Pipeline Steel,” *J. Iron Steel Res. Int.*, vol. 11, no. 17, pp. 73–78, 2010.
- [19] Z. Chen, X. Shao, X. Xu, and X. He, “Optimized digital speckle patterns for digital image correlation by consideration of both accuracy and efficiency,” *Appl. Opt.*, vol. 57, no. 4, p. 884, 2018, doi: 10.1364/ao.57.000884.
- [20] H. Song, “Science Foundation Ireland, MECHANICS Project, Personal communications (unpublished work),” 2020.
- [21] S. Dancette, V. Massardier-Jourdan, D. Fabrègue, J. Merlin, T. Dupuy, and M. Bouzekri, “HAZ microstructures and local mechanical properties of high strength steels resistance spot welds,” *ISIJ Int.*, vol. 51, no. 1, pp. 99–107, 2011, doi: 10.2355/isijinternational.51.99.
- [22] R. J. Devaney, P. E. O’Donoghue, and S. B. Leen, “Global and local fatigue analysis of X100 and X60 steel catenary riser girth welds,” *J. Struct. Integr. Maint.*, vol. 2, no. 3, pp. 181–189, 2017, doi: 10.1080/24705314.2017.1354155.
- [23] L. M. Chaboche, *Mechanics of solid materials*, vol. 19, no. 1. Cambridge University Press, 1992.
- [24] R. E. Reed-Hill, *Physical metallurgy principles*, 2nd ed. D. Van Nostrand Company, 1973.
- [25] S. Sakai and T. Sakai, “The Effect of Strain Rate, Temperature and Grain Size on the Lower Yield Stress and Flow Stress of Polycrystalline Pure Iron,” *Tetsu-to-Hagane*, vol. 58, no. 10, pp. 1438–1455, 1972, doi: 10.2355/tetsutohagane1955.58.10_1438.

- [26] S. Sakui, “The Effect of Grain Size on High Temperature Plastic Deformation of Polycrystalline Pure Iron. ,” *Tetsu-to-Hagane*, vol. 40, no. 3, pp. 263–269, 1975, [Online]. Available: https://doi.org/10.2320/jinstmet1952.40.3_263.
- [27] B. L. Mordike and P. Haasen, “The influence of temperature and strain rate on the flow stress of α -iron single crystals,” *Philos. Mag.*, vol. 7, no. 75, pp. 459–474, 1962, doi: 10.1080/14786436208212178.
- [28] S. Alhassani, “The effects of high strain rates on material properties,” Health Service Executive, UK, 1992.
- [29] Todinov, “Generic Solutions for Reducing the Likelihood of Overstress and Wearout Failures,” in *Risk-Based Reliability Analysis and Generic Principles for Risk Reduction*, vol. 1, no. 1991, Elsevier, 2000, pp. 239–263.
- [30] R. Yonezu, “Estimation method of residual stress and plastic strain in austenitic stainless steel by single indentation test,” in *Recent Advances in Structural Integrity Analyses: Proceedings of the International Congress*, 2014, pp. 555–559.

Tables

Table 1: X100 PM and cross-weld (CW) tensile and DIC test programme.

| Test | Cross-head speed (mm/min) | DIC sample frequency (Hz) | Instron sample frequency (Hz) |
|------|---------------------------|---------------------------|-------------------------------|
| PM1 | 0.35 | 0.2 | 1 |
| CW1 | 0.35 | 0.2 | 1 |
| PM2 | 0.35 | 0.2 | 1 |
| PM3 | 0.035 | 0.1 | 1 |
| CW2 | 2.1 | 2 | 1 |

Table 2: Block diameter and lath width estimates for X100 PM and FGHAZ.

| Material | d (μm) | w (μm) |
|----------------|-----------------------|-----------------------|
| PM | 5.40 | 0.685 |
| FGHAZ (10 K/s) | 4.48 | 0.606 |
| FGHAZ (30 K/s) | 4.66 | 0.613 |

Table 3: Fitted parameters for NLKIH model and Kocks-Mecking dislocation density evolution model for PM, WM, FGHAZ, and ICHAZ.

| Parameter | PM | WM | FGHAZ | ICHAZ |
|-------------------------------|--------------------|--------------------|--------------------|--------------------|
| σ_0 (MPa) | 350 | 215 | 340 | 300 |
| c_1 (MPa) | 190971 | 461825 | 277009 | 93847 |
| γ_1 | 665.3 | 2295.1 | 1365.8 | 383.4 |
| c_2 (MPa) | 1108963 | 80729.8 | 549456.8 | 54530 |
| γ_1 | 4817 | 361 | 1627 | 1457 |
| b_1 | 3.96 | 0.089 | 5.603 | 1.62 |
| Q_1 (MPa) | -160 | -55 | -110 | -75 |
| b_2 | 0.235 | 0.55 | 0.514 | 0.22 |
| Q_2 (MPa) | -115 | -60 | -85 | -33 |
| k_1 | 0.38 | 2.47 | 1.97 | 1.28 |
| k_2 | 674 | 1950 | 939 | 1000 |
| ρ_0 (mm^{-2}) | 7.47×10^7 | 4.18×10^8 | 5.36×10^6 | 5.31×10^6 |

Table 4: Fitted Coffin-Manson parameters for PM, WM, FGHAZ, and ICHAZ.

| Parameter | PM | WM | FGHAZ | ICHAZ |
|---------------|--------|--------|--------|--------|
| ϵ'_f | 0.127 | 0.177 | 2.901 | 0.212 |
| c | -0.545 | -0.526 | -0.811 | -0.479 |

Table 5: Comparison of key material properties from tensile tests for PM and cross-weld samples.

| Material | 0.1% YS (MPa) | UTS (MPa) | Total elongation (%) |
|--------------------|----------------------|------------------|-----------------------------|
| PM1 (0.35 mm/min) | 820 | 894 | 22 |
| PM2 (0.35 mm/min) | 815 | 954 | 20 |
| PM3 (0.035 mm/min) | 802 | 917 | 19 |
| CW1 (0.35 mm/min) | 605 | 746 | 26 |
| CW2 (2.1 mm/min) | 503 | 755 | 27 |

Table 6: Cyclic strain concentration factors and calculated stabilised plastic strain ranges and corresponding Coffin-Manson local fatigue life predictions for PM, WM, FGHAZ, and ICHAZ regions.

| Parameter | PM | WM | FGHAZ | ICHAZ |
|--|-----------|-----------|--------------|--------------|
| Maximum stabilised $\Delta\varepsilon_p$ (%) | 0.10% | 0.65% | 0.12% | 1.26% |
| Cyclic strain concentration factor | 0.84 | 1.39 | 0.85 | 1.99 |
| Coffin-Manson predicted N_f | 12311 | 1003 | 17955 | 777 |

Figures

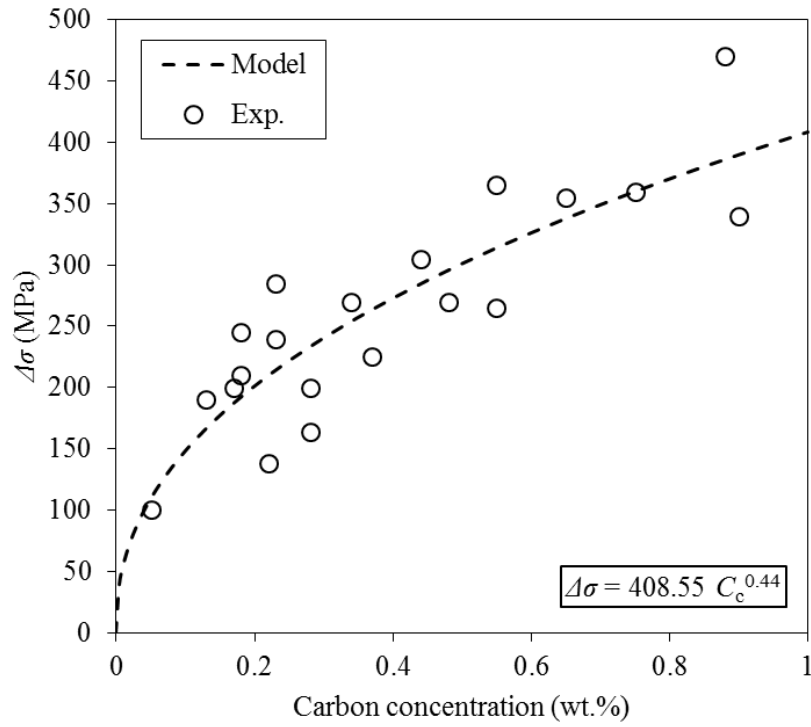


Figure 1: Strengthening contribution of interstitial carbon: comparison of AISI experimental data with fitted model.



Figure 2: Instron 4467 uniaxial test equipment and ARAMIS DIC test setup.

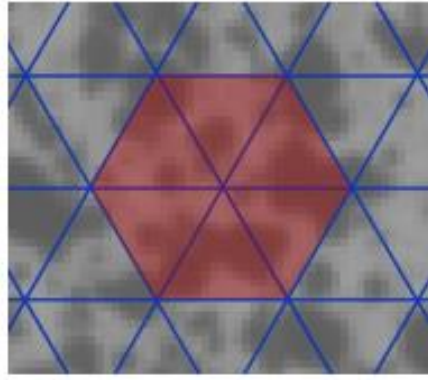


Figure 3: DIC neighbourhood, comprised of seven measurement points in ARAMIS Professional.



Figure 4: Computer-generated DIC speckle pattern printed with speckle diameter of 0.1 mm and 65% coverage.

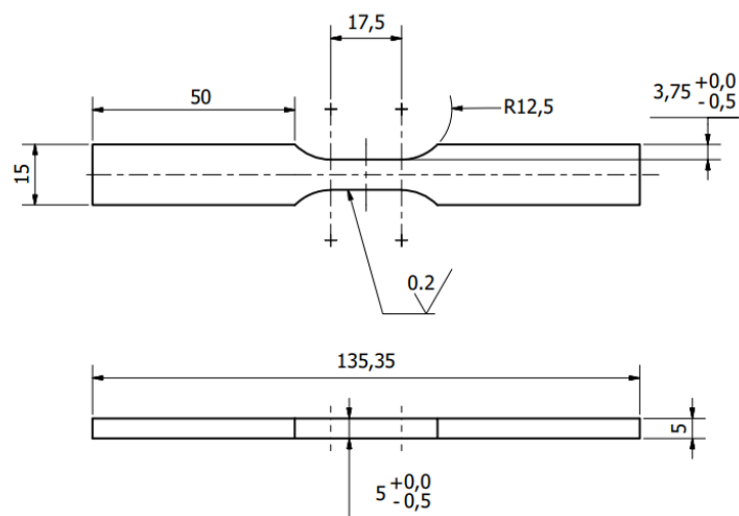


Figure 5: Test specimen technical specification.

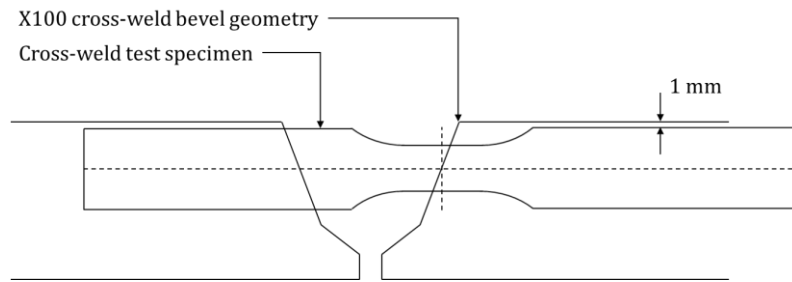


Figure 6: Cross-weld location within X100 cross-weld test specimens.

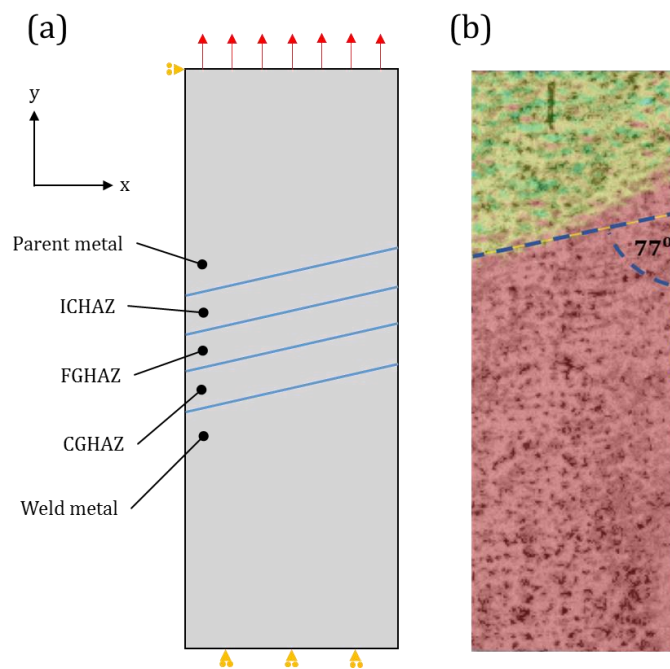


Figure 7: (a) Schematic of cross-weld geometry assumed for 2D FE model of X100 welded joint, boundary conditions, loading and material, representative of (b) DIC image of real X100 cross-weld bevel joint under low strain with demarcation of fusion boundary.

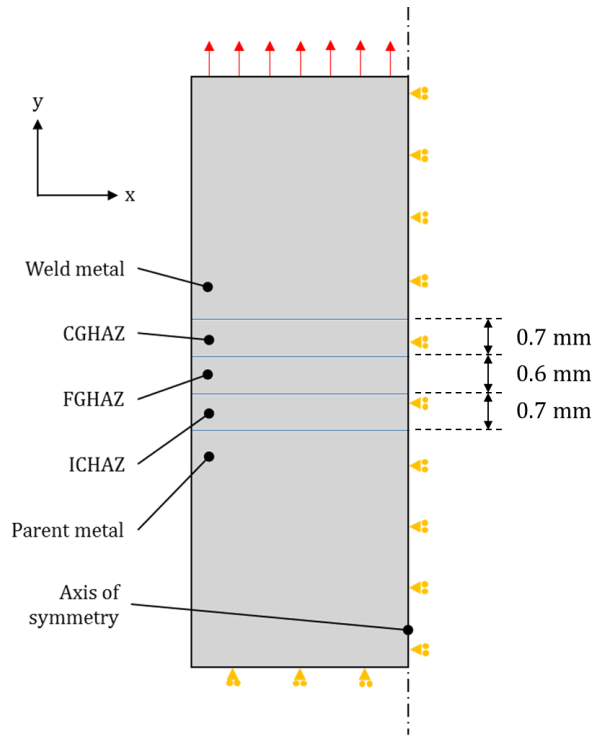


Figure 8 :2D FE model of X100 welded joint, boundary conditions, loading and material.

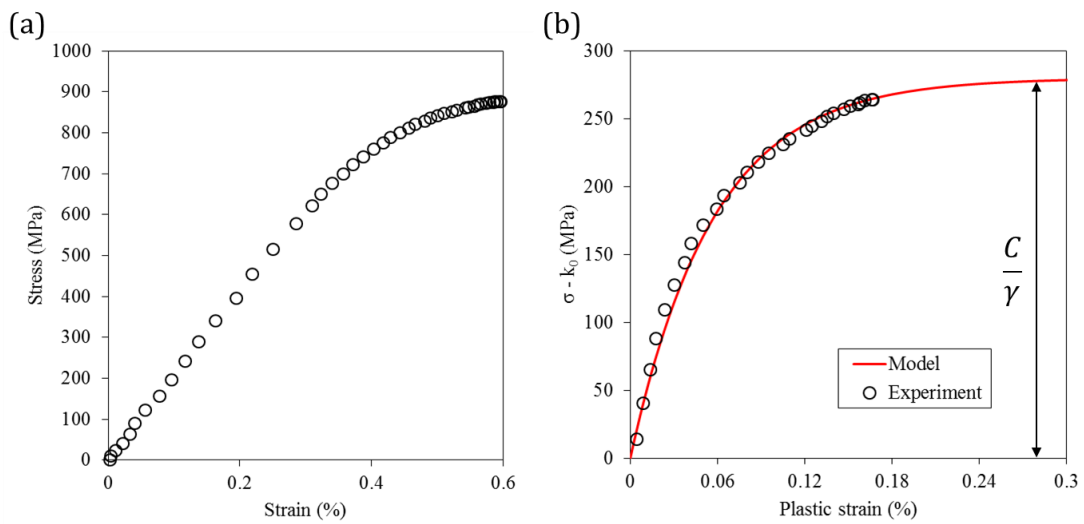


Figure 9: (a) Cyclic stress-strain data for PM and (b) Fitted kinematic hardening model to experimental data.

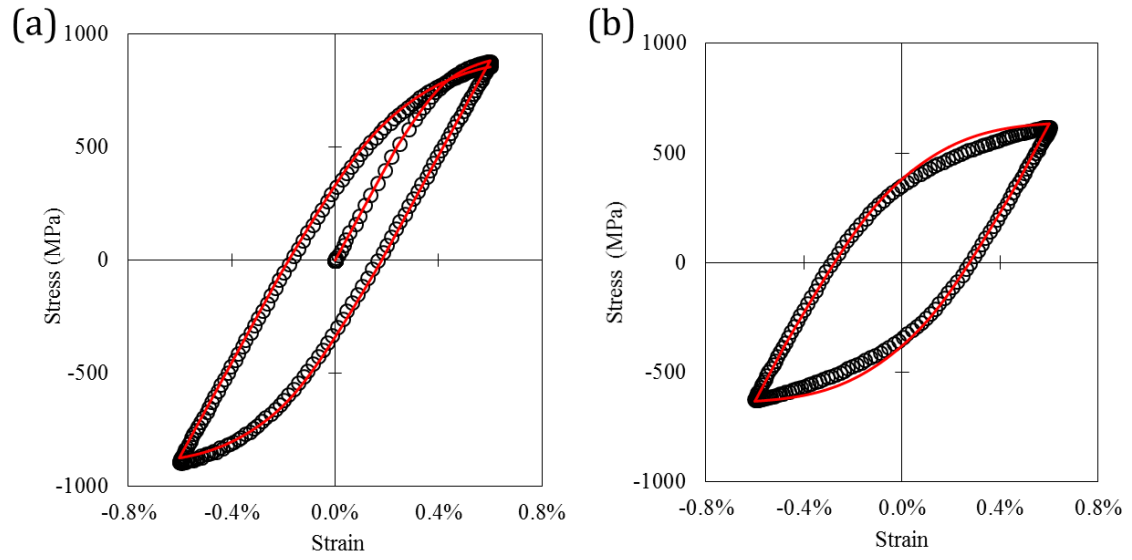


Figure 10: Comparison of experimental and modelled PM constitutive response in LCF test at a strain range of 1.2% for (a) $N = 1$, and (b) $N = N_f/2$.

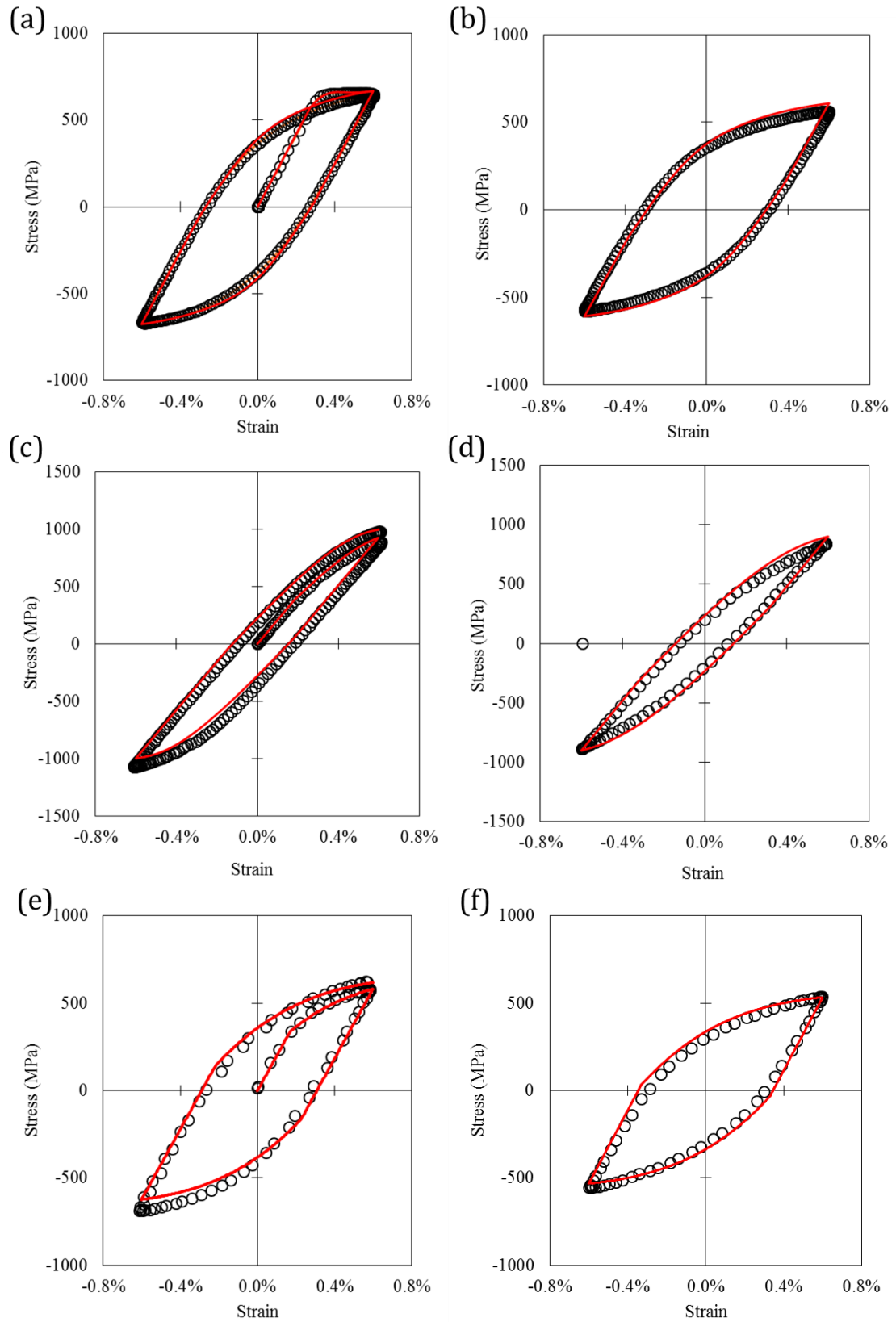


Figure 11: Comparison of experimental and modelled constitutive response in LCF test at a strain range of 1.2% for (a) WM at $N = 1$, (b) WM at $N = N_f/2$, (c) FGHAZ at $N = 1$, (d) FGHAZ at $N = N_f/2$, (e) ICHAZ at $N = 1$, (f) ICHAZ at $N = N_f/2$.

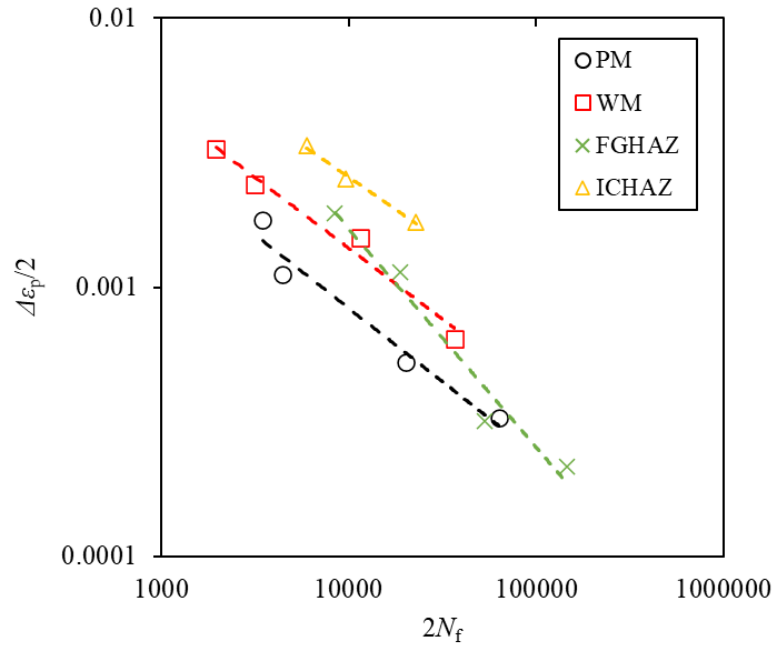


Figure 12: Fitted Coffin-Manson models for PM, WM, FGHAZ, and ICHAZ.

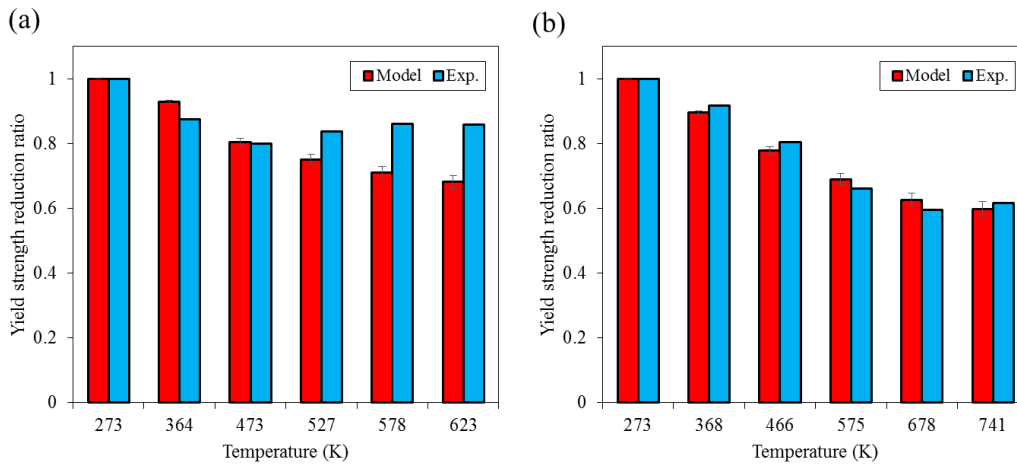


Figure 13: YS reduction ratio at various temperatures for strain-rates of (a) 0.1 s-1 and (b) 450 s-1: comparison of model with published data for S35C steel [28].

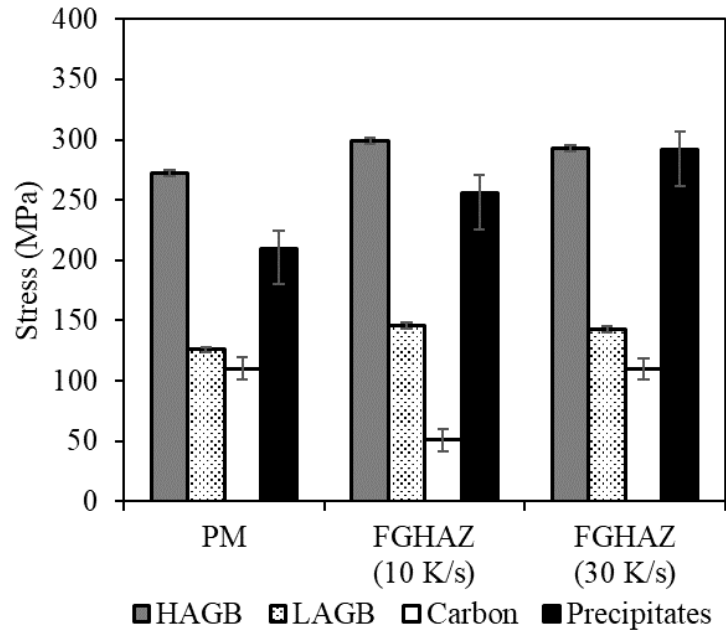


Figure 14: YS contributions of major strengthening mechanisms for PM, FGHAZ (10 K/s), and FGHAZ (30 K/s).

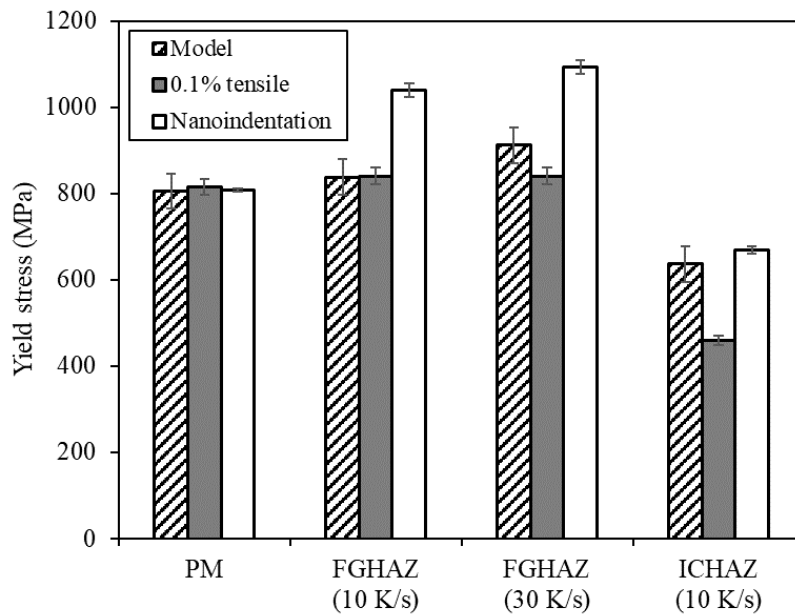


Figure 15: Comparison of predicted and experimental YS results. The ICHAZ nanoindentation result is for as-welded case; all other HAZ results are based on physically-simulated materials.

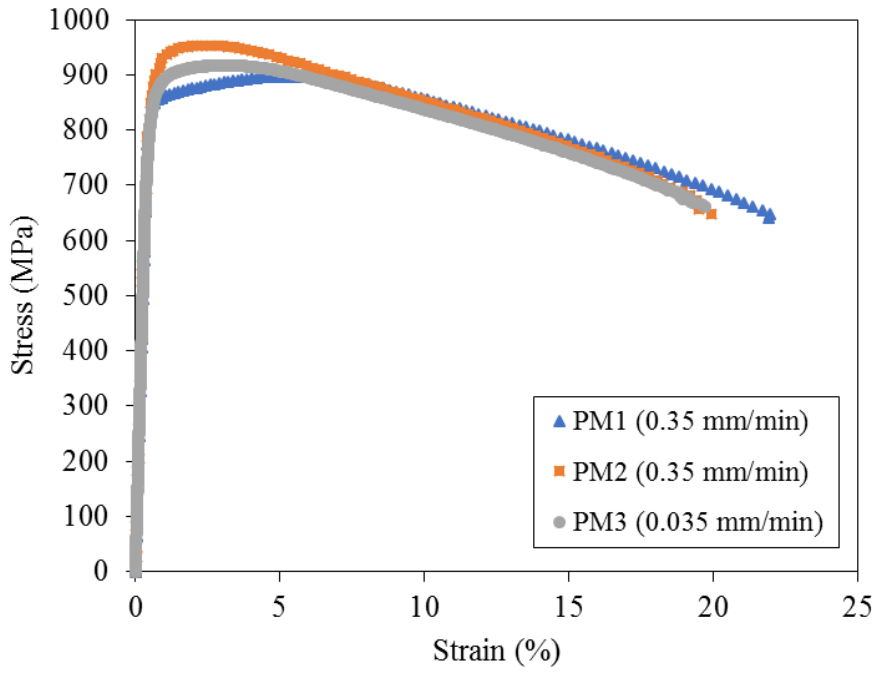


Figure 16: Comparison of X100 PM stress-strain curves at two cross-head speeds.

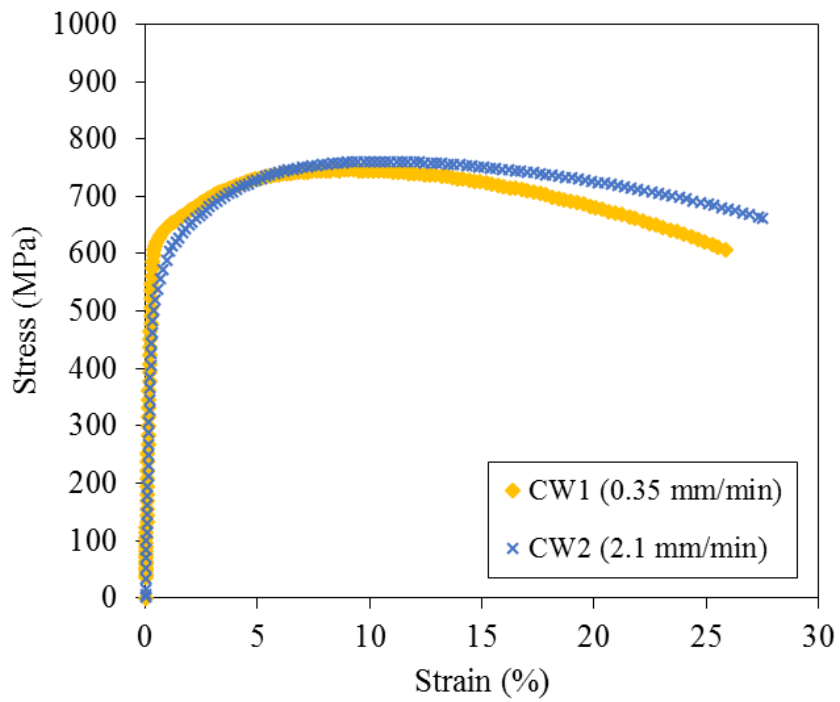


Figure 17: Comparison of X100 cross-weld stress-strain curves at two cross-head speeds.

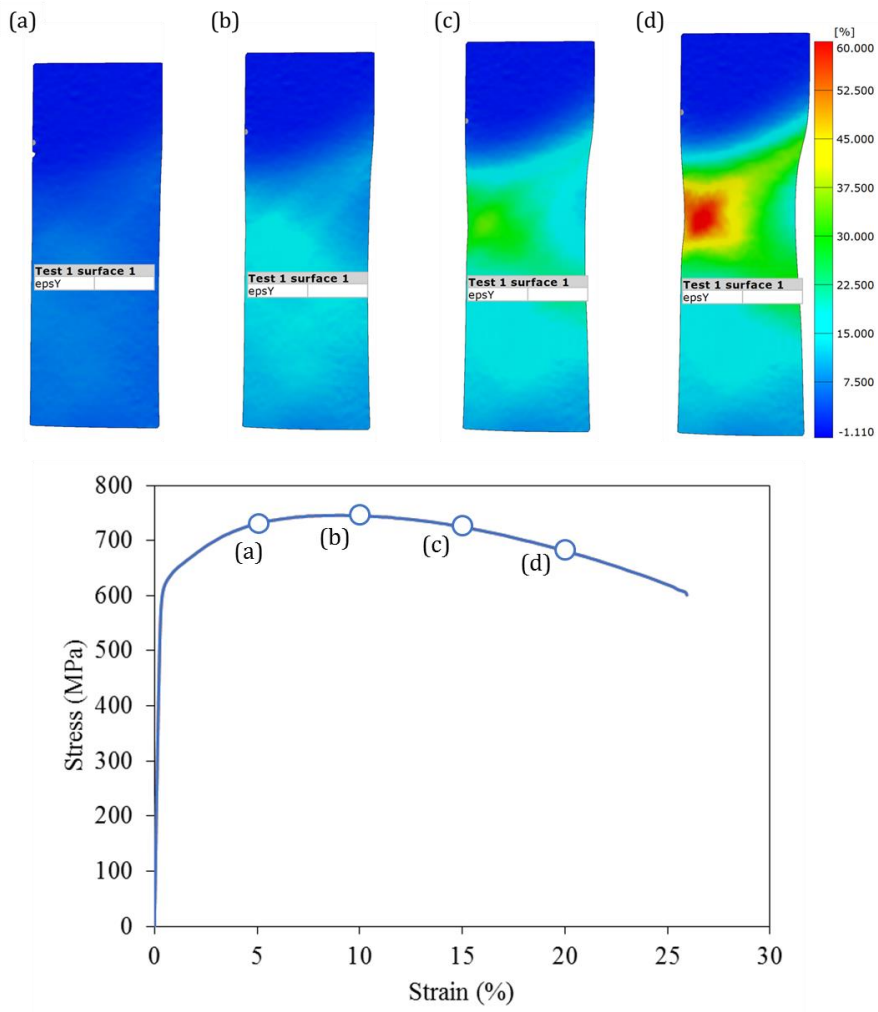


Figure 18: DIC loading-direction strain field for X100 cross-weld (test CW1) during tensile testing.

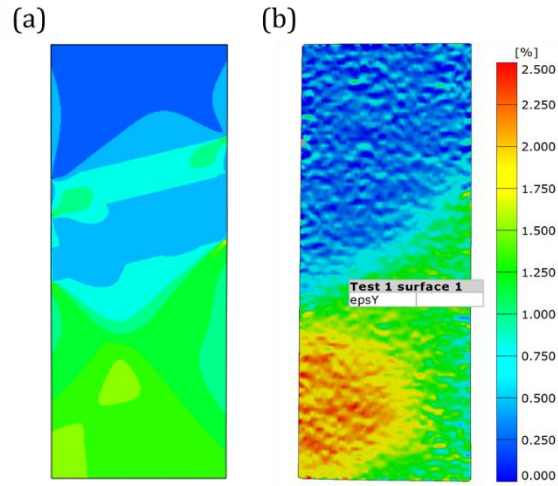


Figure 19: Comparison of loading direction strain-field in X100 cross-weld (a) FE simulation and (b) DIC tensile test at applied strain of 1.5%.

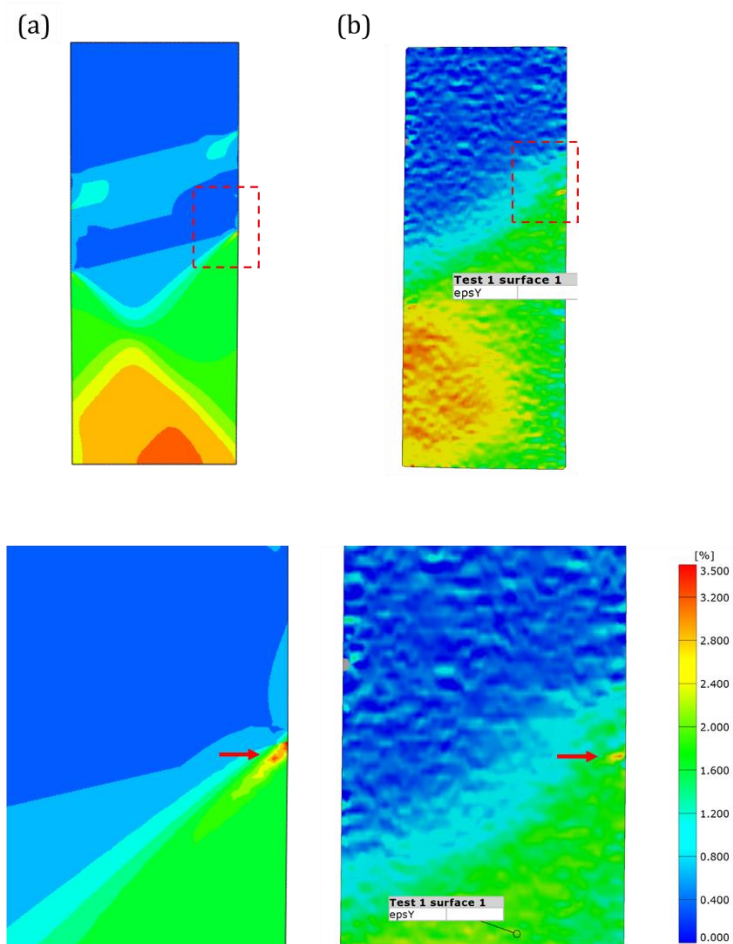


Figure 20: Comparison of loading direction strain-field in X100 cross-weld (a) FE simulation and (b) DIC tensile test at applied strain of 2%.

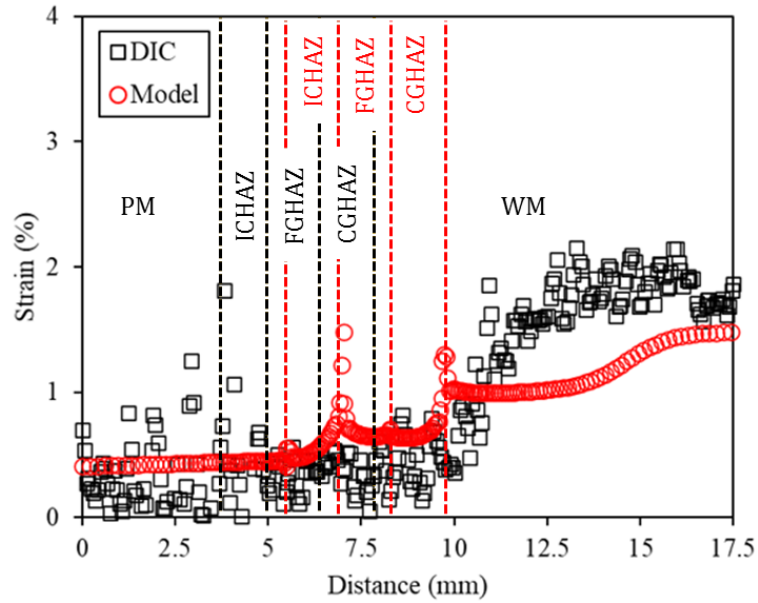


Figure 21: Comparison of predicted and measured strain distribution along left edge of cross-weld test specimen at applied strain of 1.5%.

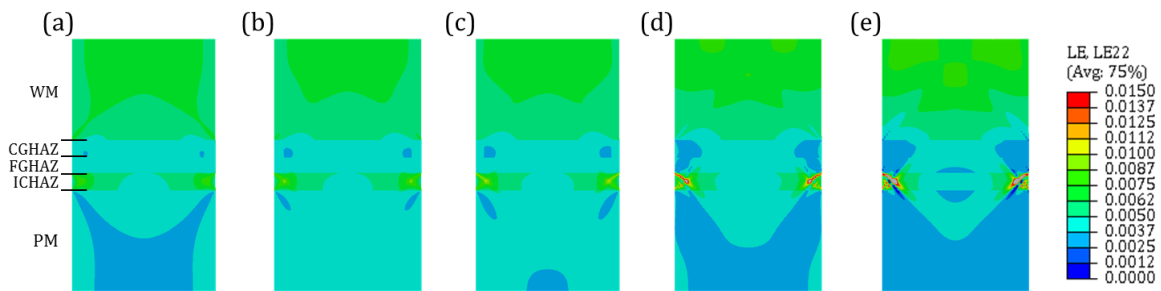


Figure 22: Tensile loading direction strain distribution in X100 cross-weld LCF simulation at $N =$ (a) 1 cycle, (b) 10 cycles, (c) 20 cycles, (d) 50 cycles, (e) 100 cycles.

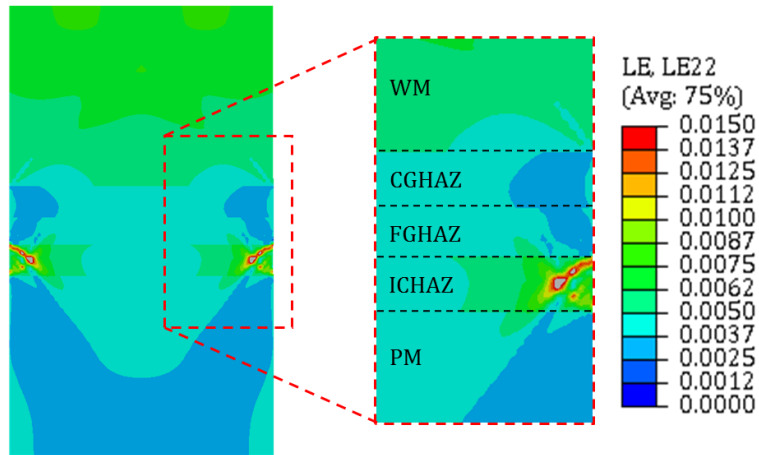


Figure 23: Magnified tensile loading direction strain distribution in X100 cross-weld LCF simulation at $N = 50$ cycles.

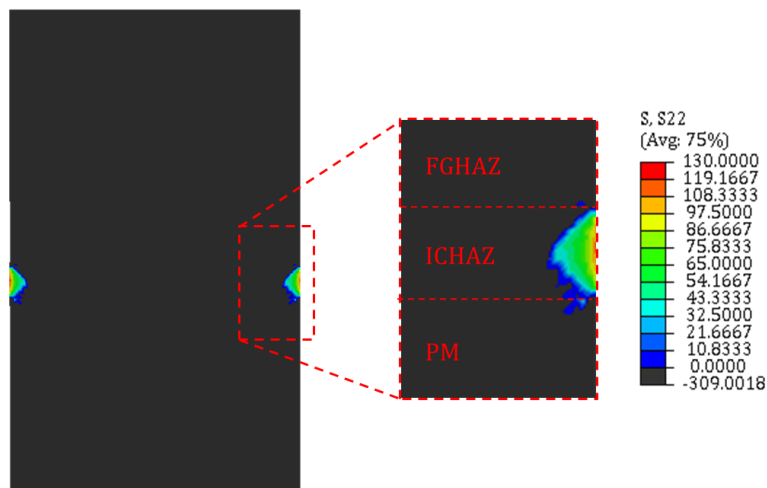


Figure 24: Magnified compressive loading direction stress distribution in X100 cross-weld LCF simulation at $N = 50$ cycles, indicating region with tensile residual strains. Dark region indicates compressive stress.

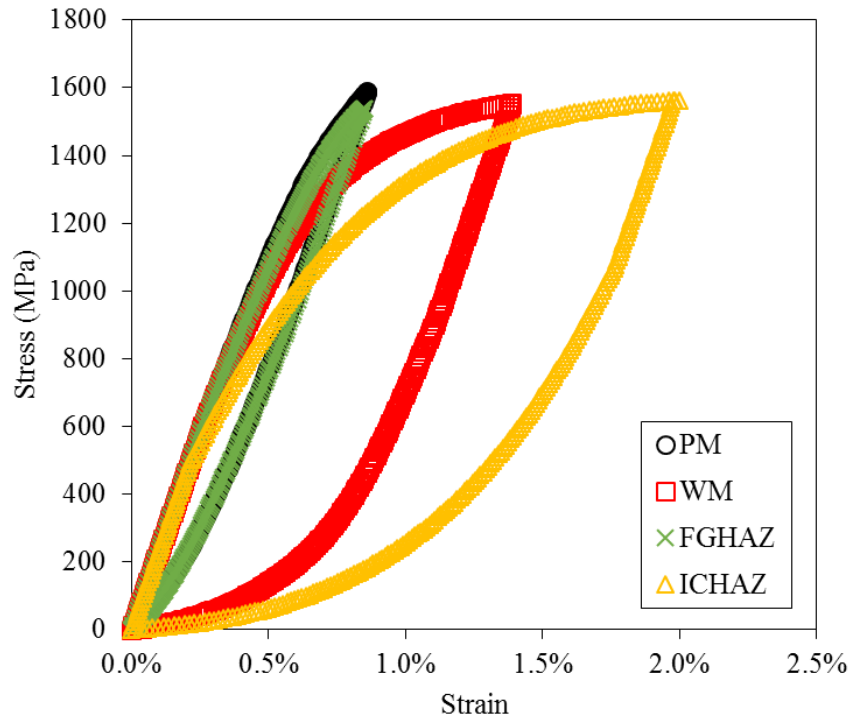


Figure 25: Nodal stabilised LCF stress-strain cycles for PM, WM, FGHAZ, and ICHAZ from LCF simulation in regions of maximum strain.

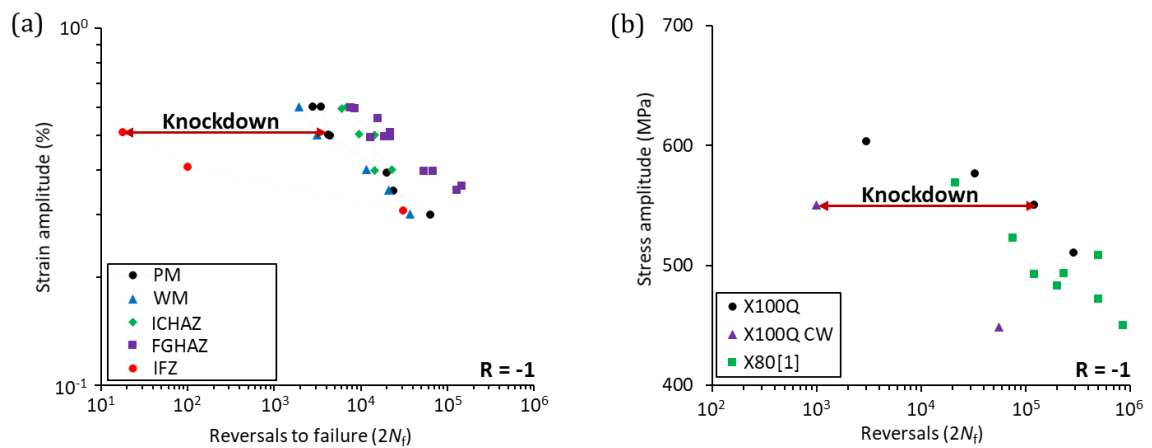


Figure 26: Illustration of fatigue life knockdown in multi-material (welded) case compared with (a) weld joint constituent materials in LCF tests and (b) X100 PM and X80 PM in HCF tests.